Shock-Induced Structural Phase Transition, Plasticity, and Brittle Cracks in Aluminum Nitride Ceramic

Paulo S. Branicio,[1,2] Rajiv K. Kalia,[1] Aiichiro Nakano,[1] and Priya Vashishta[1]

[1]*Collaboratory for Advanced Computing and Simulations, Department of Chemical Engineering and Materials Science, Department of Physics & Astronomy, and Department of Computer Science, University of Southern California, Los Angeles, California 90089-0242, USA*

[2]*Departamento de Física, Universidade Federal de São Carlos, São Carlos, São Paulo 13565, Brazil*

Atomistic mechanisms of fracture accompanying structural phase transformation (SPT) in AlN ceramic under hypervelocity impact are investigated using a 209×10^6 atom molecular-dynamics simulation. The shock wave generated by the impact splits into an elastic wave and a slower SPT wave that transforms the wurtzite structure into the rocksalt phase. The interaction between the reflected elastic wave and the SPT wave front generates nanovoids and dislocations into the wurtzite phase. Nanovoids coalesce into mode I cracks while dislocations give rise to kink bands and mode II cracking.

Hypervelocity impact damage in high performance ceramic coatings and tiles poses a real threat to satellites, spacecrafts, and space stations when they are hit by micrometeoroids traveling at speeds up to 40 km/s. At such high speeds, experimental studies are extremely difficult, and so the nature of hypervelocity impact damage in ceramics is largely unknown. In the absence of experimental information, numerical simulations are critical to the study of hypervelocity impact on high-strength ceramics. The central issue in understanding atomistic mechanisms of hypervelocity impact damage is the interplay between shock waves and material inhomogeneities that are created by extremely high stress and thermal gradients [1–4]. Mechanisms in certain ceramics, such as SiC [5] and AlN [6,7], may be highly complex because they undergo structural phase transformations (SPT) at high pressures.

Until now, experiments and computer simulations of shock have largely focused on ductile materials. State-of-the-art lasers can generate shock waves with pressures exceeding 100 GPa and temperatures of more than 10 000 K [8], while high performance light gas guns [9] can accelerate projectiles up to 16 km/s and induce pressures and temperatures in the same range. Shock experiments with lasers and gas guns reveal complex plastic deformations, structural phase transformations, void nucleation and coalescence, and spallation in metals [10–12]. Large-scale molecular-dynamics (MD) simulations on metallic systems have also provided valuable insight into shock-induced plastic deformation [13,14] and structural transitions [15]. However, it is well known that mechanical response and damage mechanisms of brittle materials are completely different from those in ductile materials [16]. Therefore what is lacking, and is essential for the design of damage tolerant ceramic coatings, is the mechanistic understanding of shock-induced damage and cracking.

The simulation presented in this Letter focuses on high strain rate deformations in an AlN slab of dimensions 150 nm × 150 nm × 100 nm. Before impact, the crystal-line structure of the target material is wurtzite. The z axis, parallel to the [0001] orientation of the wurtzite crystal, is chosen as the impact direction. Periodic boundary conditions are imposed in the x and y directions, while the target has two free surfaces perpendicular to the z axis. The projectile is a hexagonal cylinder, 15 nm wide and 30 nm long, with an initial impact speed of 15 km/s. Altogether the target and the projectile contain $\sim 209 \times 10^6$ atoms. The interatomic potential in the projectile is chosen so that the elastic moduli of the projectile are 5 times stiffer and its atomic masses are 5 times larger than those of the target. The interparticle potential between the target and projectile atoms is purely repulsive. The 627×10^6 equations of motion are numerically integrated at each time step using a time step of 1.5 fs.

The forces between atoms in the AlN target are calculated from a many-body interatomic potential, which is validated by experimental results on lattice constants, elastic moduli, cohesive energy, and melting temperature [17]. A more stringent validation is provided by the wurtzite-to-rocksalt SPT in AlN. High-pressure experiments reveal that this SPT occurs at ~ 20 GPa [18] and the calculated value is 25 GPa. The MD results for the unstable stacking fault energy and the unstable twinning energy are within 10% and 17% of the electronic structure calculations [19].

Upon impact, the projectile tip rapidly compresses the target surface [Fig. 1(a)], releasing a large amount of energy $\sim 7.8 \times 10^7$ eV nm^{-2} ps^{-1} into the target. The resulting high local energy density causes localized melting and vaporization [20–22], and creates large gradients in pressure and temperature. During the first picosecond of penetration, the projectile deforms as it loses kinetic energy and generates a shock wave whose peak pressure and speed are 100 GPa [23] and 19 km/s, respectively. The shock wave propagates almost isotropically, since the longitudinal sound speed in AlN is nearly the same in all the directions. Wherever the pressure of the shock-wave front reaches a critical value of 25 GPa, the material undergoes a
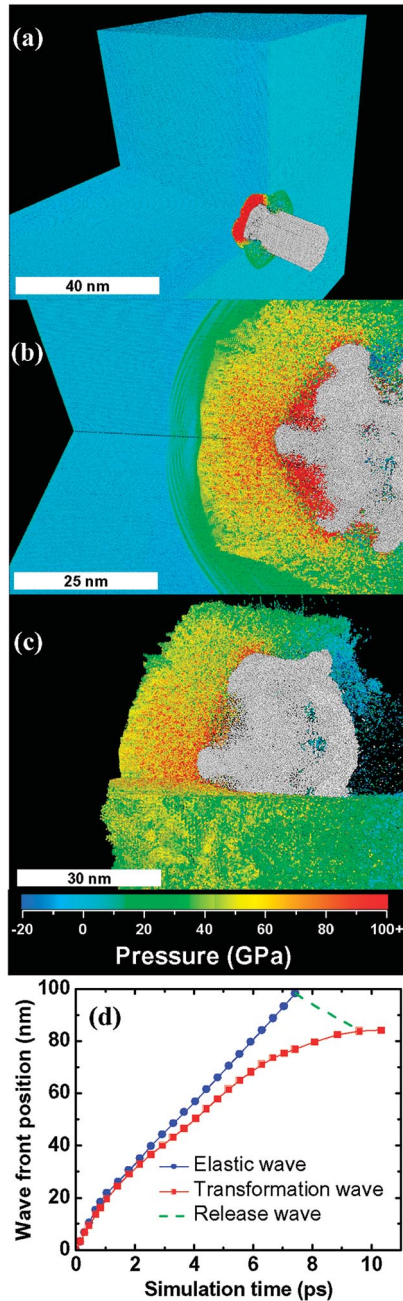
FIG. 1 (color). Shock-wave evolution during the hypervelocity impact of a $1/2 \times 10^6$ atom projectile on a 209×10^6 atom AlN ceramic target (150 nm $\times$ 150 nm $\times$ 100 nm) at an impact speed of 15 km/s. (a) Initial shock wave at time 0.675 ps, where the projectile atoms are shown in gray and AlN target atoms are color-coded according to the local pressure. Only a 3/4 cut of the target is shown to visualize the internal pressure distribution. The projectile is impacting the target from the right side. (b) Splitting of the initially overdriven shock wave into an elastic precursor (in light green) and a structural transformation wave (in dark green) at 5.325 ps. (c) Only 6-coordinated atoms in the target are shown to delineate the rocksalt region and define the morphology of the transformation wave front. (d) Wave front positions as a function of time, showing the increasing splitting of the shock wave into the elastic (blue) and transformation (red) wave fronts. The green line shows the front of the release wave reflected from the back surface of the target.

transformation from the fourfold-coordinated wurtzite structure to the sixfold-coordinated rocksalt structure [24]. This SPT accompanies the shock wave as long as the pressure is above the critical value. In about 10 ps, the shock wave slows down significantly and the SPT stops when the peak pressure drops below the threshold value of 25 GPa. The elastic compression wave continues to travel through the system at an average speed of 12 km/s.

The pair correlation function and bond angle distribution for the sixfold-coordinated atoms [25] show that the material behind the transformation wave has a nearly perfect rocksalt structure, whose density is 19% higher than that of the original wurtzite lattice. The large change in volume and lattice mismatch between the wurtzite and rocksalt structures create tensile stresses at the interface of the two structures. Figure 1(b) shows that the nearly spherical SPT wave nucleates rocksalt grains in different directions, giving rise to heterogeneous grain structures of different sizes and orientations. Consequently, the SPT wave front (i.e., the wurtzite-rocksalt interface) has a rough morphology due to defect generation and heterogeneous stress distribution [Fig. 1(c)]. Along the penetration path, the compression of the wurtzite crystal along the [0001] direction steadily increases the atomic coordination from the fourfold- to the sixfold-coordinated rocksalt structure along one of the three equivalent atomic displacement paths in the {0001} plane. A cross section of the rocksalt phase along the projectile penetration path shows clearly the presence of grains with the [100] rocksalt direction aligned with the original [1$\bar{1}$00], [10$\bar{1}$0], and [01$\bar{1}$0] wurtzite directions.

In our simulation, two independent mechanisms of crack nucleation and growth are identified, both rooted at the wurtzite-rocksalt interface, which is a favorable spot for stress concentration and defect generation. When the compressive wave is reflected from the back free surface of the target, a tensile wave is generated in the reverse direction [see the dashed line in Fig. 1(d)]. Upon reaching the wurtzite-rocksalt interface, the tensile wave and the stresses due to lattice mismatch at the interface cleave Al-N bonds in the {1$\bar{1}$00} planes, nucleating nanoscale voids in the interfacial region where the tensile stress is maximum [pointed out by the arrow in Fig. 2(a)]. The tension at the interface then triggers crack growth from these nanovoids into the wurtzite crystal [26]. Cracks propagate along the [0001] direction from the SPT boundary in mode I (opening mode) [see Figs. 2(b) and 2(c)] cleaving {1$\bar{1}$00} planes to release tension.

Another set of defects is dislocations at the wurtzite-rocksalt interface due to interaction with release waves. The impact direction, [0001] in the wurtzite crystal, is perpendicular to the basal plane, which is the primary slip plane for dislocations [27]. Since the planes of the highest shear stress due to localized pressure do not coincide with the basal plane, the shear stress is released through a series of dislocation dipoles with opposite Burgers vectors in the basal plane forming a kink band
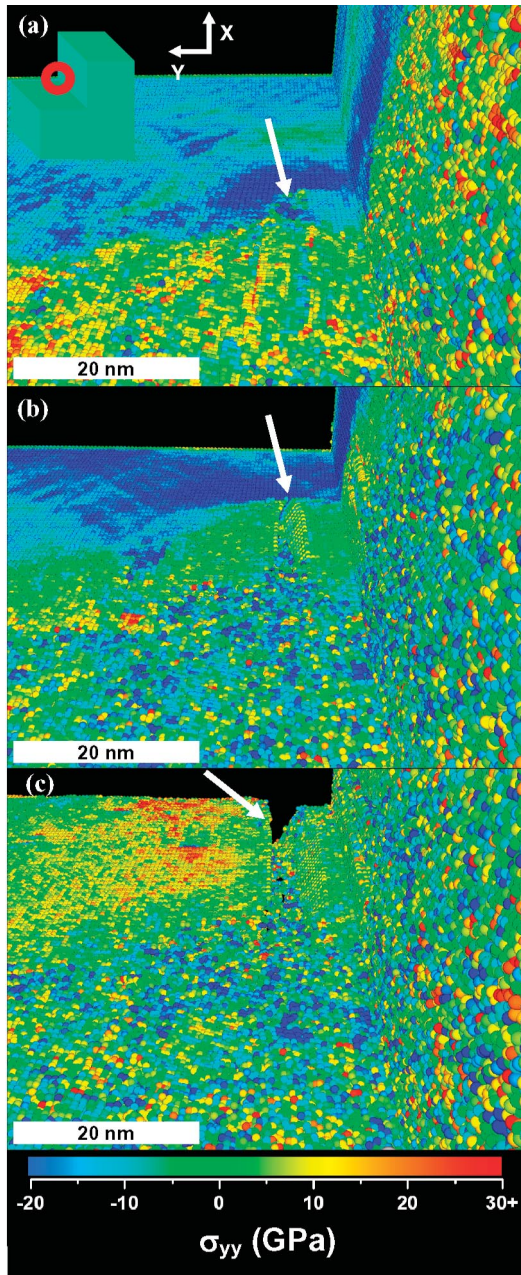
FIG. 2 (color). Nucleation of a crack from a nanocavity near the wurtzite-rocksalt interface, caused by the interaction with a tensile wave reflected from the back surface of the target. Only part of the 3/4 cut of the target in Fig. 1 is shown, at the location marked by the red circle in the inset. The atoms are color-coded according to the σ_{yy} component of stress. (a) Tensile wave traveling in the wurtzite crystal reaches the rocksalt interface and starts to nucleate a nanocavity, shown by the arrow, at time 10.05 ps. (b) Cleavage of the wurtzite crystal by the crack nucleated from the nanocavity, propagating towards the back surface of the target (pointed by the arrow) at time 12.0 ps. (c) The crack reaches the back surface at time 16.95 ps.

FIG. 3 (color). Nucleation and development of a kink band at the wurtzite-rocksalt interface. Atoms are color-coded as in Fig. 2. Only the $(1\bar{1}00)$ plane of the wurtzite crystal cut along the middle part of the target is shown; see the red circle in the inset. (a) Snapshot taken at 11.1 ps shows the kink band nucleates at the interface and grows into the wurtzite crystal, generating dipoles of edge dislocations (shown by the arrows) of opposite Burgers vectors in the basal plane and propagating in the $[11\bar{2}0]$ direction. (b), The development of the kink band at 15.3 ps, with the movement of dislocations, forms a region with tilted crystallographic direction inside the crystal, shown by the red arrows. Note that the coupling of dislocations (superdislocation), shown with the white arrows, forms a nearly perfect tilt boundary. (c) A 3-dimensional representation of the dislocation structure in (b) shows loops opening in the basal plane as the kink band expands. (d) The tilt boundary is a stress concentrator. It causes a mode II shear fracture with a small mode I component by displacing the grains and releasing the tensile shear stress at 31.5 ps.

[28] [crystalline region with a different crystallographic orientation from the surrounding; see Fig. 3(a)]. The kink band nucleates at the SPT wave front and extends into the defect-free wurtzite crystal [Figs. 3(a) and 3(b)]. Disloca-

tion dipoles in the kink band are, in fact, closed dislocation loops [29] [Fig. 3(c)]. Dislocation lines at the boundary of the kink band can move easily in the basal plane. To maximize rotation and stress release, the dislocations on one side of the kink band align to form a superdislocation [28] [Fig. 3(b)] and a high-angle tilt boundary that glides to the edge of the system [Figs. 3(b) and 3(d)]. Cracks are nucleated along the superdislocation boundary of the kink bands, and propagate mainly in mode II (shearing mode), releasing the shear stress due to localized expansion. A small mode I component is also present, as evidenced by grain detachment perpendicular to the direction of crack propagation; see Fig. 3(d). Figure 4 shows cracks generated by both mechanisms at time 31.5 ps.

Experimentally, two major types of crack patterns, i.e., radial and cone cracks, are often observed during impact damage in ceramics [30–33]. The atomistic mechanisms discussed above can account for these two types of crack patterns, if the appropriate stress profiles are taken into consideration. Radial cracks can be associated with the superposition of tangential stresses from the spherical propagation of the compressive shock wave and release waves from the free surface. Cone cracks can be associated
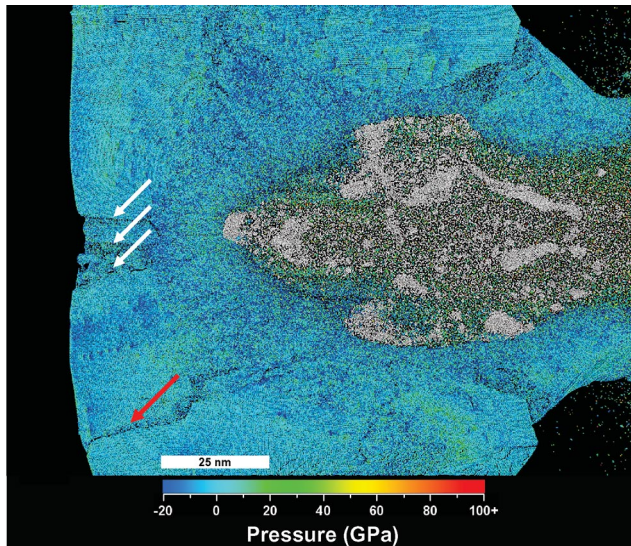
FIG. 4 (color). AlN target after 31.5 ps from initial impact showing the multifractured configuration. Arrows indicate fractures cleaved from defects formed in the interface of the wurtzite and rocksalt structures. The red arrow indicates fracture in mode II, while the white arrows indicate fractures in mode I. Several other fractures, not discussed in the text, are also cleaved from similar mechanisms in the front surface of impact.

with the accumulation of shear stress, which generates rotational plasticity before crack nucleation. Dislocation loops, locks, twins, and kink bands are frequently observed in metallic systems. In brittle high-strength ceramics, failure generally occurs with little plastic deformation except at high temperatures or high compression [27–34], where rotational plasticity is activated if dislocations are not free to glide because of barriers (e.g., grain boundaries, impurities, or dislocation locks) or misalignments between dislocation glide planes and planes of high shear stress. The MD simulation reported here sheds light on atomistic mechanisms for the initiation of nanocavities leading to mode I cracking as well as for kink band formation and mode II cracking at the SPT boundary during hypervelocity impact in AlN ceramic.

[1] D. H. Robertson, D. W. Brenner, and C. T. White, Phys. Rev. Lett. **67**, 3132 (1991).

[2] C. T. White, D. H. Robertson, and D. W. Brenner, Physica (Amsterdam) **188A**, 357 (1992).

[3] *Handbook on Materials Modeling*, edited by S. Yip (Springer, Berlin, Germany, 2005), Vol. 39.

[4] R. J. Hemley and N. W. Ashcroft, Nature (London) **380**, 671 (1996).

[5] F. Shimojo *et al.*, Phys. Rev. Lett. **84**, 3338 (2000).

[6] M. Ueno *et al.*, Phys. Rev. B **45**, 10 123 (1992).

[7] M. E. Kipp and D. E. Grady, J. Phys. III (France) **4**, C8-249 (1994).

[8] M. Koenig *et al.*, Phys. Rev. E **50**, R3314 (1994).

[9] L. C. Chhabildas, L. N. Kmetyk, W. D. Reinhart, and C. A. Hall, Int. J. Impact Eng. **17**, 183 (1995).

[10] G. I. Kanel *et al.*, *Shock-Wave Phenomena and the Properties of Condensed Matter* (Springer, New York, 2004).

[11] J. A. Ang and B. D. Hansche, in *High Pressure Shock Compression of Solids II: Dynamic Fracture and Fragmentation*, edited by L. W. Davison, D. E. Grady, and M. Shahinpoor (Springer, New York, 1996), p. 176.

[12] W. Chen and G. Ravichandran, J. Am. Ceram. Soc. **79**, 579 (1996).

[13] N. W. Ashcroft, Nature (London) **340**, 345 (1989).

[14] B. L. Holian and P. S. Lomdahl, Science **280**, 2085 (1998).

[15] K. Kadau, T. C. Germann, P. S. Lomdahl, and B. L. Holian, Science **296**, 1681 (2002).

[16] J. R. Rice and R. M. Thomson, Philos. Mag. **29**, 73 (1974).

[17] For the functional form of interaction, see J. P. Rino *et al.*, Phys. Rev. B **70**, 045207 (2004).

[18] T. Mashimo *et al.*, J. Appl. Phys. **86**, 6710 (1999).

[19] Fuyuki Shimojo (private communication).

[20] A. B. Belonoshko, Science **275**, 955 (1997).

[21] B. L. Holian, Phys. Rev. A **37**, 2562 (1988).

[22] R. M. Brannon and L. C. Chhabildas, Int. J. Impact Eng. **17**, 109 (1995).

[23] For calculation of stress, see K. S. Cheung and S. Yip, J. Appl. Phys. **70**, 5688 (1991).

[24] Pressure and stresses are virial values calculated from atomic positions and velocities, and averaged over a sphere of 0.25 nm around each atom. Appropriate time and space averages are equivalent to measurements.

[25] Coordination is the number of neighbor atoms within a sphere of radius 0.25 nm.

[26] A. A. Griffith, Phil. Trans. R. Soc. A **221**, 163 (1920).

[27] V. Audurier, J. L. Demenet, and J. Rabier, Philos. Mag. A **77**, 825 (1998).

[28] A. E. Romanov and V. I. Vladimirov, in *Dislocations and Disclinations*, edited by F. R. N. Nabarro (North-Holland, Amsterdam, 1992), Vol. 9, p. 191.

[29] Nanovoids and dislocation loops were obtained from the shortest-path ring of alternating Al-N atomic bonds. In the perfect AlN structure, atoms have 12 shortest-path rings with 6 members. Around dislocations, the number of the six-member rings per atom is lower than that and on the nanovoids-crack surface, the number drops to 50% of the bulk value.

[30] M. W. Chen, J. W. McCauley, and K. J. Hemker, Science **299**, 1563 (2003).

[31] D. Sherman, Int. J. Impact Eng. **24**, 313 (2000).

[32] E. Strassburger *et al.*, J. Phys. IV (France) **10**, PR9-605 (2000).

[33] E. Strassburger, H. Senf, and H. Rothenhausler, J. Phys. IV (France) **4**, C8-653 (1994).

[34] M. Azzaz, J. P. Michel, V. Feregotto, and A. George, Mater. Sci. Eng. B **71**, 30 (2000).